

RF TEST BENCHES FOR ELECTRON CLOUD STUDIES

F. Caspers, J-M. Laurent, U.Iriso Ariz, A. Mostacci
CERN, Geneva, Switzerland

Abstract

In the framework of the CERN program on the electron cloud effects, two laboratory Radio Frequency (RF) set-ups have been built to study and characterize the phenomena by complementing one to the other. The first consists in a coaxial test stand with a 100 mm diameter vacuum chamber forming the outer conductor and 6 wires cage-aerial-type as the inner conductor. In order to simulate the bunched beam, this test stand is powered with short pulses. The available field strength in a travelling wave mode allows triggering electron multipacting in stainless steel surfaces, but not in chambers treated to reduce the secondary emission yield. Thus, upgrades in the bench set-up have been pursued: instead of dumping the pulsed power into a load, it is re-circulated in a multiple frequency ring resonator. For this purpose, we designed a directional coupler with several kV DC isolation, very low transmission losses and a bandwidth of 4 octaves.

In the second set-up, multipacting is produced in a resonator consisting in a coaxial wave guide (1.5 m long) shunted at both ends: the inner conductor diameter is 32 mm while the outer conductor diameter amounts to 100 mm. Due to the standing wave configuration, high electromagnetic fields are stored inside the set-up, and multipacting is 'one point type'. This is rather different than the one taking place in accelerators, but electron surface bombardment is large enough to produce and characterize the scrubbing effect. An overview of the present status of both set-ups is given here, highlighting the latest improvements and results.

1. THE TRAVELING WAVE MULTIWIRE CHAMBER

1.1. Introduction: the need of a Ring Resonator

Multipacting is an electron multiplication resonance, which develops in RF devices when a periodic field strength is maintained between two opposite surfaces and if energy and resonant conditions for electron kinetics are met. Such conditions will show up in the Large Hadron Collider (LHC). The bunched proton beam will provide the periodic electric field; an electron cloud may develop leading to vacuum breakdown by a fast pressure increase and potentially ending in important degradation in beam performance and/or excessive liquid helium consumption.

In order to study those phenomena in a laboratory, a bench test set-up [1] was built where six wires are

inserted in a circular vacuum chamber and submitted to RF pulses simulating the Transverse Electro-Magnetic (TEM) field produced by a bunched beam (Fig. 1). That travelling wave (TW) coaxial structure is powered by a wideband power amplifier* driven from a pulse generator. The output is connected to a RF load, which absorbs the transmitted power and prevents undesirable reflections. Two probes have been installed to collect the electrons, one placed on top of the chamber and the second one is the pick-up shown in Fig. 1.

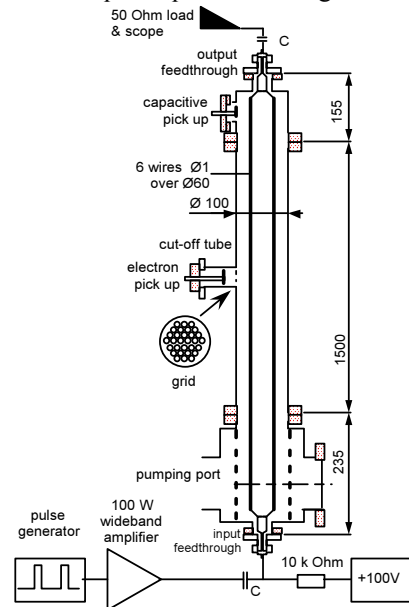


Figure 1. TW multi-wire chamber. The pulses coming from the signal generator are amplified up to 100 V by the wideband power amplifier. The pulse, biased to ensure a positive voltage, travels along the six wires inside the chamber. The 50 Ω RF load on the top avoids undesirable reflections. The capacitors on top and bottom isolate the DC currents inside the chamber. Lengths are given in mm.

The achievable electric field strength is mainly limited by the output power of the wideband amplifier. On the 50 Ω load, the initial (i.e. before improvements) output voltage, V_{IN} , is limited to 100 V (baseline-peak), which corresponds to multipacting electron energy $E_e^{m} = 75$ eV, according to both simulations and measurements in [1]. To trigger multipacting, the Secondary Emission Yield (SEY) has to be greater than 1.3 [2]. A typical characteristic for baked-out stainless steel surfaces is shown in Fig. 2, from where it is clear that 75 eV is sufficient to trigger multipacting. The SEY behaviour

* Amplifier research, Model 100W1000, 1-1000 MHz, 100 W.

for “treated” chambers is similar as what is shown in Fig. 2 for bake-out stainless steel, except that the minimum multipacting energy is pushed further. On top of that, this energy increases also after that the material has been exposed to a certain electron dose. For materials common in accelerator technology, the minimum multipacting energy can be moved up to the 200 eV range. Therefore it is desirable to reach higher multipacting energies in the bench test stand.

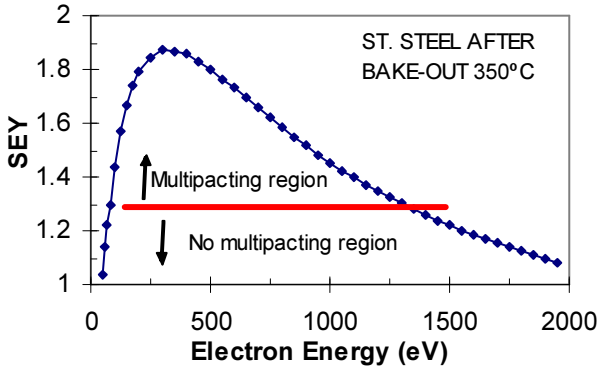


Figure 2. Secondary Emission Yield (SEY) for stainless steel after bake-out (data measured by Y. Bojko, CERN-LEP-VAC, 1996). Multipacting occurs only when the SEY is above the horizontal line (i.e. SEY greater than 1.3).

A possible way to increase the voltage V_{IN} (without changing the amplifier), is to re-inject a fraction of the output power into the system, similarly to what is proposed in [3]. Such a re-circulating scheme is called Ring Resonator (RR) and allows a much more efficient use of the amplifier output power.

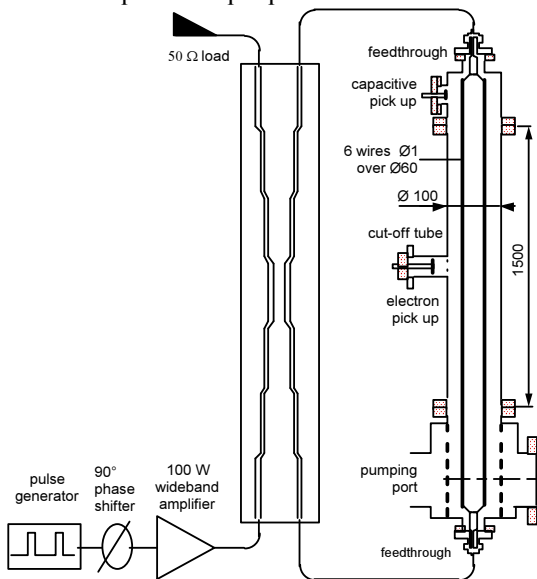


Figure 3. Ring resonator outline. Pulses from the signal generator are amplified in the power amplifier, and introduced in the wideband directional coupler. Part of the pulse is dumped at the end of one arm of the

coupler to the RF load, while the other arm sends the induced signal to the chamber. When leaving the chamber, the pulse enters again in the coupler, where it is added to the next pulse delivered by the amplifier. The phase shifter compensates the 90° phase offset produced by the coupler. On top of the chamber there is a button probe, which will be used to evaluate the power enhancement effect of the RR.

The conceptual scheme is shown in Fig. 3: the pulse coming from the chamber and the pulse coming from the amplifier are superimposed by means of a directional coupler. The RF pulses coming from the signal generator are amplified in the power amplifier, and then introduced in the wideband directional coupler. Part of the pulse power is dumped to the RF load, while another part enters into the chamber. When leaving the chamber, the pulse again goes through the coupler, where it is added to the next pulse delivered by the amplifier. The 90° phase shifter between the signal generator and the power amplifier, compensates the 90 deg. offset introduced by the coupler.

The RR has stringent requirements: low reflection from the Travelling Wave transmission line and a RF coupler designed “ad hoc”. The final goal is to get a gain for the incident power around 8 or 9 dB (sec. 1.2), i.e. nearly 10 times the amplifier output power. In the following we report about the necessary steps to build the RR: improvements on the TW chamber (sec. 1.3) and design and test of the coupler (sec. 1.4). Achieved performances are given as well (sec. 1.5).

1.2. Loop power gain

In a RR, the (maximum) power gain (G) is given by [4]

$$G = \left[\frac{C}{1 - 10^{-\alpha/20} \sqrt{1 - C^2}} \right] \quad (1)$$

where C is the voltage coupling factor of the coupler and α is the one-way attenuation in the ring (in dB). Figure 4 sketches the power gain as a function of the attenuation for different values of C . To get a useful gain ($G \sim 8-9$ dB), a possible choice is $\alpha \sim 0.5$ dB and $C \sim 10$ dB (circle in Fig. 4). Those conditions have to be maintained up to a maximum frequency f_{MAX} given by the relative bandwidth of the coupler (i.e. $BW=20$ from previous experience) and by the minimum working frequency, $f_{MIN}=30$ MHz (corresponding to the 25 ns bunch spacing of LHC plus a “contingency margin”): $f_{MAX} = BW * f_{MIN} = 600$ MHz. The one way attenuation α depends mainly on the reflection coefficient and the transmission losses in the TW chamber (sec. 1.3), while the voltage coupling factor is a specification of the coupler (sec. 1.4).

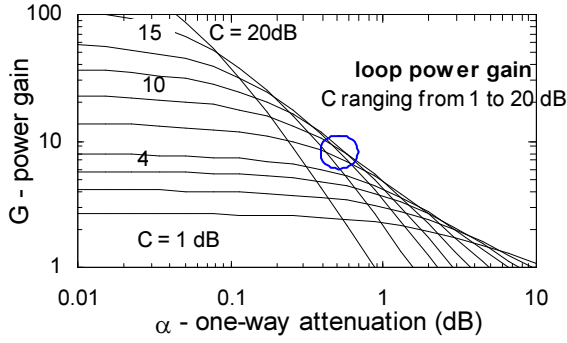


Figure 4. Power gain in the ring resonator (G) as a function of the attenuation in the ring (α) and the voltage coupling factor C . The circle marks a possible choice of parameters: $\alpha \sim 0.5$ dB and $C \sim 10$ dB to get a power gain G between 8 and 9 dB.

1.3. Improvements to the original chamber

Reducing the one way attenuation (α) requires acting both on the transmission losses of the six wires in the (circular) vacuum chamber and on the impedance matching among cables, feedthroughs and the coaxial structure (i.e. reducing reflections). The frequency response of the initial set-up has been measured with a Vector Network Analyzer (HP8753D), as shown in Fig. 5 (transmission coefficient versus frequency) and Fig. 6 (characteristic impedance (Z_{line}) along the structure). These plots compare the initial situation (dotted lines) to the improved one (solid lines). The initial transmission coefficient is plotted in Fig. 5 (dotted line) showing that it has to be further reduced (at least up to f_{MAX}). Using the time domain option (step mode) of the instrument, the reflection coefficient Γ can be measured as a function of the position along the coaxial line. Then from

$$Z_{line} = Z_0 \frac{1 + \Gamma}{1 - \Gamma}, \quad (2)$$

one gets Z_{line} along the transmission line, as shown in Fig. 6. Ideally, the characteristic impedance should be 50Ω all along the path, in order to avoid reflections. The dotted line (original status) indicates impedance mismatches at the feedthrough locations as well as along the wire (minor effect). The transition pieces, joining the wires to the feedthroughs, have been electrically and mechanically redesigned (Fig. 7 is a sketch of the relevant geometry). The joint is made of Cu and the Cu-Be transition star has been gold plated in order to reduce its contact resistance and to improve the welding properties. The diameter of the different parts of the joint is chosen according to

$$Z = 60 \ln \left(\frac{D_{ext}}{D_{int}} \right), \quad (3)$$

while their heights (h) are such that $h \cong D_{ext} / 9$ in order to provide a smooth RF transition [4]. On one side of the chamber, the six Cu wires are crimped and welded

on the transition stars arms, while on the other side they are fixed by clamps. The diameter of the circle formed by the six wires (60 mm in our case) has been optimised following experimental results (no analytical approach is available). Special feedthroughs, taken from the LEP Standing Wave Cavities (LEP SWC), have been also used for UHV performance and mechanically robustness in order to resist the mechanical tension of the wires.

All these improvements produced the effect seen in figures 5 and 6 (solid lines). The transmission coefficient is now within the correct limits (0.5 dB at 600 MHz), since the impedance is close to 50Ω all along the line, except at the unavoidable transition between the 6 wires structure and feedthroughs. Anyway, according to the measurements, this residual mismatch causes no significant losses in α .

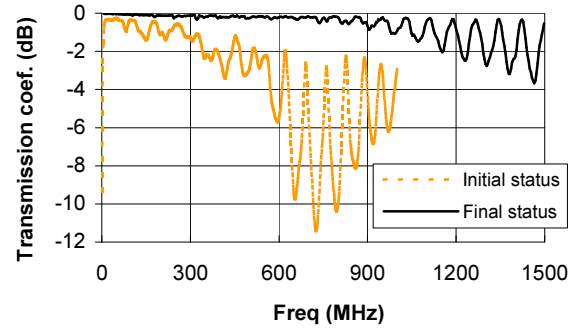


Figure 5. Transmission coefficient of the TW chamber before (dotted orange line) and after (solid black line) the improvements described in sec. 1.3. The transmission coefficient is within desired limits: 0.5 dB up to 600 MHz.

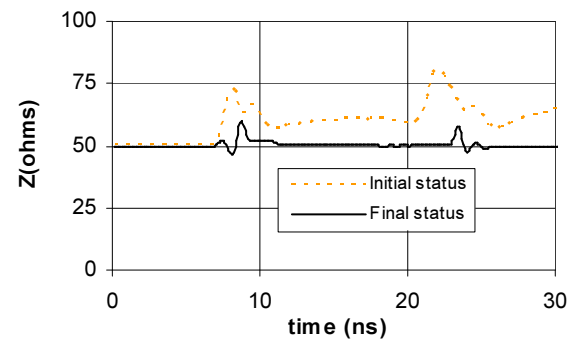


Figure 6. Characteristic impedance along the chamber before (dotted orange line, upper trace) and after (solid black line) the improvements described in sec. 1.3. Eventually, the impedance along the line is everywhere close to 50Ω except for the unavoidable residual mismatches after the feedthroughs (transition from the feedthroughs to the 6 wire structure), which do not affect significantly the transmission coefficient.

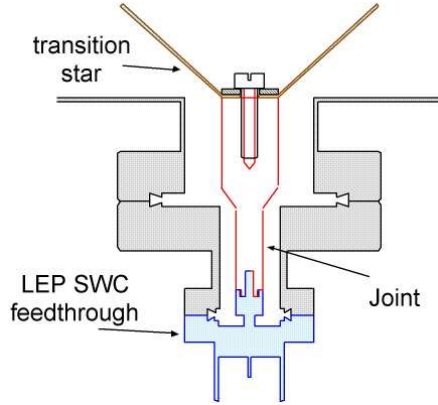


Figure 7. Bottom part of the chamber, where we can see the transition pieces between the feedthroughs and the six wires. The joint is made of Cu, while the transition star is made on Cu-Be. The transition star has six arms, corresponding to the six inner wires, but only two of them are drawn here.

1.4. Coupler design.

As stated above, the coupler should have a voltage coupling factor $C = 10$ dB in the whole frequency range. On top of that, the coupler must stand DC isolation up to 1 kV between the strip-lines and ground (according to multipacting simulations). The lowest working frequency (f_L) is fixed by the spacing between the RF pulses. Since the aim is to simulate LHC bunches, where the bunch spacing can go up to $\Delta T = 50$ ns, the lowest relevant frequency is $f_L = 1/\Delta T = 20$ MHz (with reduced performances). The upper frequency limit (f_{MAX}) is set to 600 MHz as explained in sec. 1.2.

The $\lambda/4$ symmetric 9 sections coupler described in [5] accomplishes our requirements. Since the central frequency is 300 MHz, each section is $\lambda/4 = 25$ cm, which implies a coupler length ~ 2.25 m (see Fig. 8). Due to the non standard specifications, the coupler has been built “ad hoc” using copper strips 0.3 mm thick (to reduce ohmic losses) and bending them as shown in Fig. 8 (right picture). Such a “U-like shape” is repeated for each section, varying its characteristic lengths: x , w , u , l , and s . The dimensions of the shielding box are chosen according to the cut-off frequency of the high order propagating mode (i.e. 1 GHz for our structure).

The voltage coupling factor depends on the characteristic impedance for the odd and even TEM propagating modes (Z_{odd} and Z_{even}). The free design parameters are the geometrical dimensions (defined in Fig. 8): they are carefully determined to meet the required value of Z_{odd} and Z_{even} for each section [6]. For a given geometry (i.e. a set of values for x , w , u , l , and s) the odd and even impedances are first computed with *SuperFish*, a 2-D electrostatic computer code wide used in RF accelerating cavities [7], and then measured on a special test stand. This procedure has been then repeated for each section.

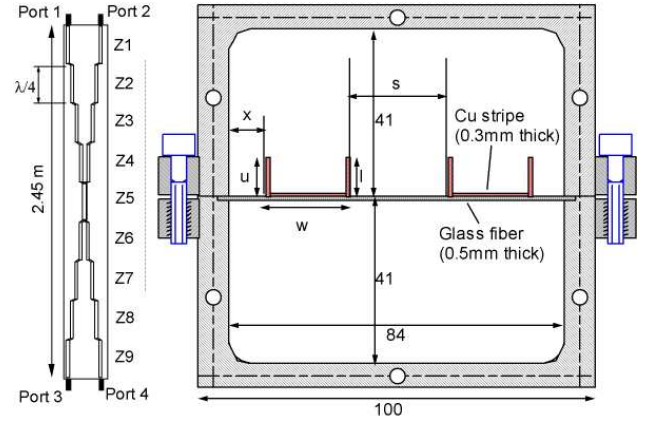


Figure 8. Top view (left picture) and cross section (right picture) of the coupler. The left side shows the layout of the coupler with the nine sections (referred as Z_i with $i=1, \dots, 9$). Since the coupler is symmetrical, $Z_j = Z_{10-j}$ ($j=1, \dots, 4$). The right picture shows the copper stripes parameters (w , u and l) and their positions (x and s) that change for each section to have the appropriate values of the impedance. All distances are given in mm.

The *SuperFish* simulation works as follows. The two strips are (numerically) excited both with a voltage $+V$ (even mode) or one with $+V$ and the other with $-V$ (odd mode). The code computes the energy stored inside the box for each excitation (U_{odd} and U_{even}). Following the analogy with electric circuits [8], one gets:

$$Z_{odd} = \frac{2 \cdot V^2}{c \cdot U_{odd}} \quad (4)$$

and

$$Z_{even} = \frac{V^2}{c \cdot 2 \cdot U_{even}}, \quad (5)$$

where c is the velocity of light.

Each section is then tested in a dedicated coupler 50 cm long but with exactly the same cross section dimensions (the only ones important for Z_{odd} and Z_{even}). The impedance of both modes in the whole coupler are shown in Fig. 9, where the ideal (or theoretical) impedance values found in [9] are marked with red crosses. In Fig. 9, Z_{odd} and Z_{even} are measured connecting the VNA to ports 1 and 2 (Fig. 8, left) through a hybrid coupler to give a phase offset: 0 degrees for even mode measurement, 180 degrees for the odd mode measurement. The time domain (step mode) reflection data are then converted to impedance data using Eq. (2). After half of the structure, the previous data are not longer valid because of multiple reflections and the same measurement has been done from ports 3 and 4 (Fig. 8, left): the results are very similar (minor tolerances).

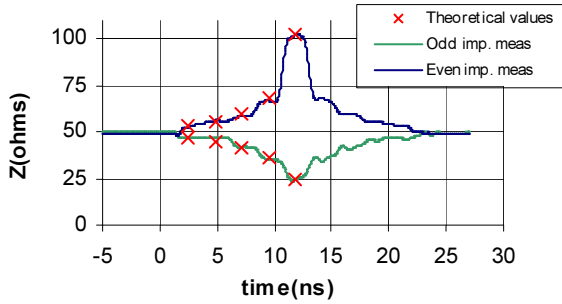


Figure 9. Z_{odd} and Z_{even} measured in the final coupler as a function of the time (i.e. position along the line). After half of the structure, measurements are not longer valid because of the measuring reflections.

Figure 10 shows the behaviour of C as a function of the frequency for three cases: the ideal one (corresponding exactly to the theoretical impedance values given in [9]), the calculated behaviour of C from Z_{odd} and Z_{even} measured for each section separately and the measurement on the whole coupler. Concerning the blue curve of Fig. 10, the coupling factor has been computed with SERENADE, while the violet curve is the transmission between ports 1 and 2 of the coupler: Actually, the coupler working range is from $f_{\text{MIN}}=20$ MHz up to $f_{\text{MAX}}=530$ MHz (instead of 30 - 600 MHz); the effects of this difference are negligible in the final RR working. The ripple in C is sensible to small variations of the characteristic impedance of each section.

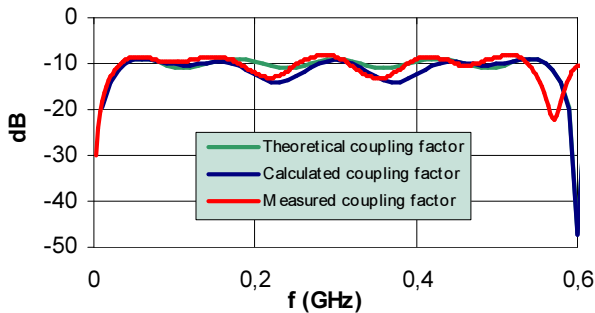


Figure 10. Coupling factor of the final coupler. The ripple of the measured coupling factor (violet line) is reasonably close to both theoretical (light blue line) and calculated (blue line) behaviour in the relevant frequency range (20 to 530 MHz, as explained in the text).

1.5. Final Ring Resonator

The final layout of the RR is shown in Fig. 3. In order to see the power enhancement effect of the Ring Resonator, we measure the transmission between a

button probe located on top of the chamber and the bottom connection of the chamber. Figure 11 compares the signals seen using the RR (black line) compared to the signal in the original TW chamber (orange line). The power enhancement occurs only at particular frequencies which are integer multiples of $f_R = 1/T_R$, being T_R the round trip time in the RR. The round trip time depends also on the length of the connecting cables and was chosen to be 25 ns, according to the nominal LHC bunch spacing. Figure 11 shows a value of f_R close to 40 MHz. The difference between the orange line (measured directly to the chamber) and the black curve (measured using the RR) shows a minimum gain at $(n \cdot f_R)$ of 6 dB, where n is a natural number.

To compensate the 90° phase offset intrinsically given by the coupler, the pulse has been “pre-distorted” with a phase shifter placed just after the source (see Fig. 3). The phase shifter enhances also the amplitude of the signal actually sent into the RR. The plot in Fig. 12 shows a gaussian unitary pulse before (orange line) and after (blue line) a 90° phase shift, as in an ideal 90° phase shifter. The amplitude of the phase shifted pulse varies from -0.65 to +0.65. Assuming that the amplifier output voltage swing is ± 1 (after normalisation), the “bipolar-like” signal is amplified by $2/1.3=1.53$, i.e. 3.7 dB. Thus the total power enhancement is $6+3.7=9.7$ dB.

Thus the available amplitude of the TW pulses can be at least 3 times bigger, which allow to produce multipacting electrons of roughly 200 eV. At this energy, typically the SEY is bigger than 1.3 (multipacting threshold) and close to its maximum (SEY_{max}).

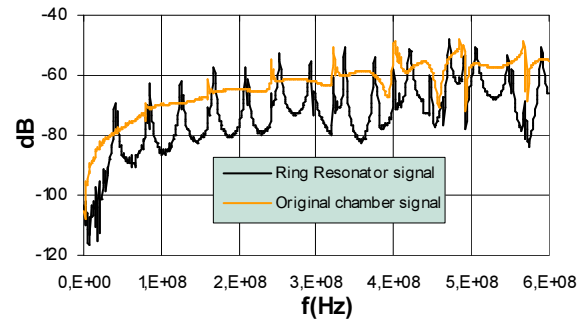


Figure 11. Amplitude of the signal seen in a button pick-up on the top of the chamber as a function of the frequency with the effect of the RR (black line) compared with the original chamber (orange line). In this plot, the maximum peaks frequency rate for the RR set-up is slightly larger than 40 MHz due to cables length.

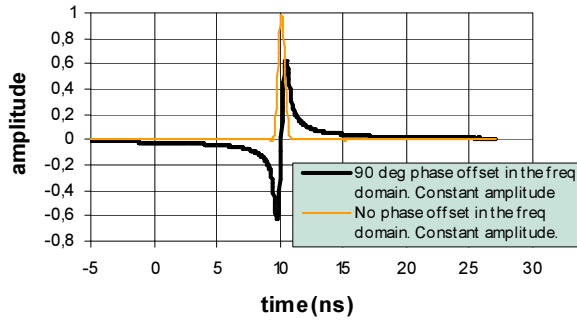


Figure 12. Effect of a 90° phase shift on a gaussian pulse. The plot shows a gaussian unit pulse before (blue line) and after (orange line) a 90° phase shift, as in an ideal phase shifter. The curves are obtained measuring with VNA (time domain, pulse mode) the transmission through a cable between port 1 and port2.

2. THE STANDING WAVES SINGLE CONDUCTOR COAXIAL CHAMBER

2.1. Introduction: motivation for a Standing Waves single conductor coaxial chamber

In an accelerator, the emitted electrons from one side of the wall cross the chamber to impact the other side of the chamber (two points multipacting). As seen in sec. 1, this can be simulated by a TW structure, but the electric field available is limited. In order to reach higher electric fields, a Standing Wave (SW) single conductor coaxial chamber has been developed and used to test multipacting. Since in a SW configuration electric field is confined inside the resonator, the electron energy and bombardment dose can be high enough to simulate accelerator conditions. Not only fully treated surface can be tested, but also the study of samples is suitable. Nevertheless, this set-up does not satisfactorily simulate the multipacting in an accelerator: in a SW configuration (due to RF sinusoidal field) the outgoing electrons from one wall may hit again the same surface after one or several complete RF cycles (one point multipacting) [10].

There are several reasons to study this effect. In fact, multipacting currents can absorb RF energy and produce breakdown in high power components, such as couplers or RF accelerator cavities (superconducting or not). It is useful to compare different surface treatments or different materials, providing a ‘calibration’ for numerical simulations.

2.2. Experimental set-up

The SW single conductor coaxial chamber is nothing else than a coaxial resonator: a 1.5 m long coaxial line shunted at both ends (with an inner diameter is 32 mm and an outer one of 100 mm). The upper end holds two adjustable magnetic couplers: one, critically coupled, for feeding RF power and the second one, weakly coupled, to measure in transmission mode the resonance frequency and the quality factor Q . The

lower plane is perforated (towards the vacuum pump) in order to allow the vacuum pumping of the resonator. A typical operational vacuum pressure is $5 \cdot 10^{-8}$ mbar. An electron pick-up is placed in the middle of the resonator where the electric field is maximum (in the fundamental mode) and thus where most of the electrons are produced (see Fig. 13). The pick-up layout depends on the actual measurement and two typical ones are discussed below.

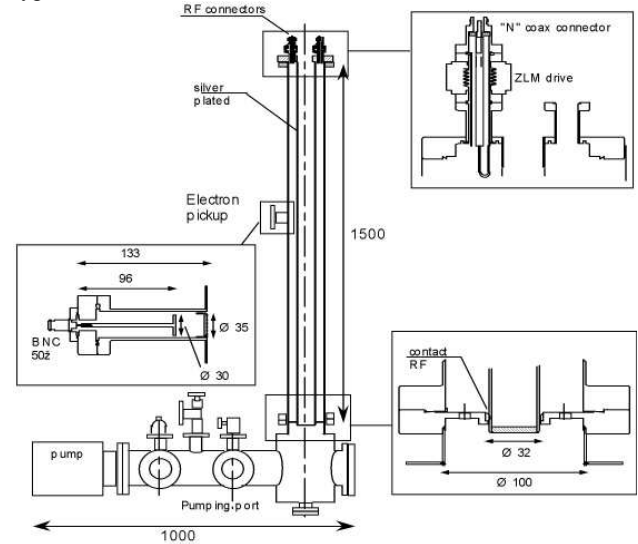


Figure 13. Layout of the coaxial resonator with details of top and bottom parts. The inner conductor is silver plated to increase its conductance, and the electron pick-up is placed in the middle of the resonator where the electric field is maximum. The upper end holds the two adjustable magnetic couplers, while the lower end is perforated to allow the vacuum pumping of the resonator. Lengths are given in mm.

The resonator is operated in the fundamental TEM mode, at a resonant frequency f_0 ($f_0=98.7$ MHz); a drift of f_0 (± 0.1 % variation) has been observed and it is mainly due to temperature, which varies with the dissipated power in the structure. As confirmed by simulations [11], multipacting is one point type and takes places in the inner surface of the outer conductor. The outer conductor is made of stainless steel while the inner conductor is silver-plated in order to improve its conductance: the field is higher there and the silver plating increases the quality factor Q of the resonator. Q_{load} is the ratio between the energy stored in the resonator and the power losses:

$$Q_{load} = \frac{f_0 W}{P_p}, \quad (6)$$

where W is the total stored energy and P_p is the power lost in the resonator, including the external coupling system (losses due to feeding couplers, transmitter, etc). For this set-up, Q_{load} has been computed from the voltage measured at the output coupler as a function of the frequency:

$$Q_{load} = \frac{f_0}{f_2 - f_1} \quad (7)$$

where f_0 corresponds to an output voltage of V_{max} , and f_2 and f_1 are the frequencies at which $V=V_{max}/\sqrt{2}$ (3 dB points). Usually when feeding power into a resonator from a RF source, part of it goes into the resonator and part of it is lost in the coupling circuit. The so called “critical coupling” is when all power goes to the resonator and no reflection occurs [12]. One can reach a condition close to critical coupling by modifying the coupling circuit (to minimise reflections). Assuming critical coupling, the Q of the resonator is twice the Q_{load} measured from the coupling circuit (in our case $Q=2*Q_{load}=760$).

The magnetic coupling loops are mounted on two manual drives, which allow adjustment of their active area. The RF power is fed to the resonant resonator via the input coupling loop. Its positioning allows to change the input coupling and obtain critical coupling (i.e. minimizing the reflected measured signal). The output loop is, instead, adjusted to observe a small signal from the electromagnetic field stored in the resonator. Both loops are placed where the magnetic field is maximum.

2.3. Electric field calibration

The maximum amplitude of the electric field inside the chamber is measured from the power stored in the resonator. The signal generator produces the input signal, which then is amplified by a 50 dB amplifier (see Fig. 14). A power meter measures the incident power to and the reflected power from the resonator.

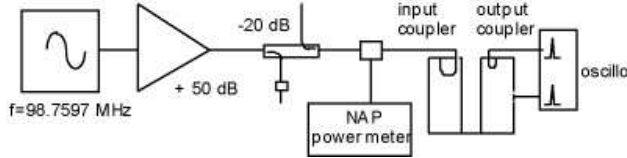


Figure 14. Layout used to measure the power inside the resonator, and thus, calculate the electric field. The signal generator sends the RF sinusoidal signal, which then is amplified (50 dB) by the power amplifier and finally introduced to the resonator via the input coupler. The power meter measures the incident and reflected power, while the power stored in the resonator is measured with the output coupler.

The voltage difference between the inner and outer conductor is given by [13]

$$u = \sqrt{P_{inside} \cdot Q_{load} \cdot Z \cdot (4/\pi)} \quad (8)$$

where P_{inside} is measured, and Z is the characteristic impedance calculated using Eq. (3).

In an infinitely long coaxial line, the electric field produced by a inner conductor with linear charge density λ is:

$$E(r) = \frac{\lambda}{2\pi\epsilon_0 r} \quad (9)$$

being ϵ_0 the vacuum dielectric constant. Analogous to what is seen in Eq. (8), the potential u can be calculated as:

$$u = \frac{\lambda}{2\pi\epsilon_0} \ln(R_{ext}/R_{int}), \quad (10)$$

with R_{ext} the internal radius of the outer conductor, and R_{int} the radius of the inner conductor.

Comparing eqs. (8, 10) and then using Eq. (9), one gets the electric field in terms of the power measured inside the resonator, i.e.

$$E(r = R_{ext}) = \frac{\sqrt{Q_{load} \cdot Z \cdot (4/\pi)}}{R_{ext} \cdot \ln(R_{ext}/R_{int})} \cdot \sqrt{P_{inside}} \quad (11)$$

This expression for the electric field is used to set the multipacting threshold of the material under study.

According to [14], the electric field that accelerates multipacting electrons in an accelerator (circular) beam pipe is

$$E = \frac{q_b}{2\pi\epsilon_0 r_{pipe} (c \cdot \Delta t_b)} \quad (12)$$

where q_b is the bunch charge, r_{pipe} is the pipe radius and Δt_b the bunch spacing. For example, assuming for the CERN-SPS a circular beam pipe, the expected electric field in the SPS and the field actually got in the bench set-up have the same order of magnitude of roughly 10^4 V/m, i.e. $P_{inside}=10$ W (10^{11} protons, 2.5cm pipe radius and 1 ns bunch length). Thus also the electron bombardment dose in the bench set-up is close to the SPS one, validating this method to test different surface treatments.

2.4. Multipacting signatures

The SW coaxial chamber allows the detection of multipacting in two different ways. Typical signatures are the sudden pressure rise, and the collection electron current at the pick up. By amplitude and frequency modulation of the input signal, it is also possible to determine how multipacting affects the resonant conditions.

2.4.1. Pressure rise

Due to Electron Stimulated Desorption (ESD), when multipacting takes place, the vacuum pressure rises depending on the electric field amplitude. The pressure is measured by a Penning vacuum gauge located on the pumping stand (Fig. 13). Thus varying the electric field amplitude, the pressure growth can be controlled, as shown in Fig. 15, where the time evolution of the pressure can be seen. The pressure increases (depending on the electric field inside) up to a factor of 8, close to the values found in accelerators [15].

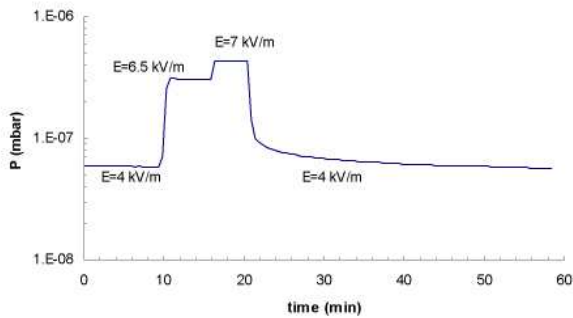


Figure 15. Pressure behaviour varying the electric field amplitude in the resonator. The working pressure is $5 \cdot 10^{-8}$ mbar, but when multipacting is triggered ($t=10$ min) the pressure suddenly increases, up to a stable value. Increasing the electric field, the pressure still increases.

2.4.2. Electron current

The multipacting electrons can be detected by the positively biased pick-up where they induce a negative signal. Varying the power in the resonator around the multipacting threshold, allows the detection of the beginning of multipacting. This threshold is usually given in terms of electric field, using Eq. (11). The electron current measured on the pick up can be also modulated by varying the amplitude of the incident power with the signal generator. This effect is shown in Fig. 16, where the incident signal was 10% modulated in amplitude around the multipacting level at a frequency of 10 Hz. For electric field amplitudes lower than the multipacting threshold, no electron current is collected, but when multipacting is active, the electron current increases when increasing the input power (i.e. the electric field in the resonator). For each input power level, the electron current is limited presumably by space charge effects.

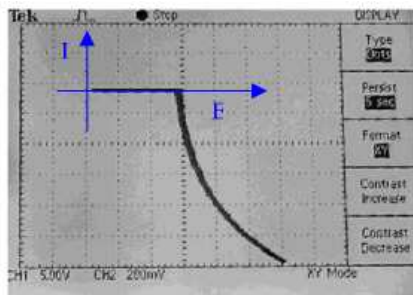


Figure 16. Electron current versus electric field (10% modulation at 10 Hz of the resonator input signal). The amplitude modulation is done using the signal generator. When multipacting takes place, electron current is detected on the pick-up. For electric field below the multipacting level, no electron current is collected.

The threshold changes depending on the material inside the resonator, as it will be seen in sec. 2.4. A

surprising effect was detected by modulating the amplitude of the electric field with at increasing frequencies. Figure 17 was recorded in the same conditions as Fig. 16, (10% amplitude modulation) but the frequency of the amplitude modulation was much faster: 100 Hz. This hysteresis cycle shows that, at least for this set-up, it is easier to maintain multipacting than to trigger it.

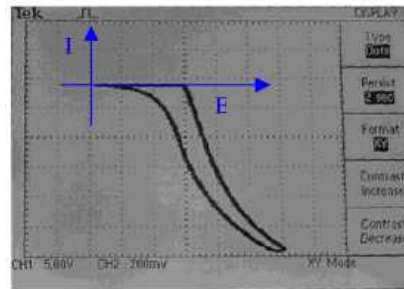


Figure 17. Electron current versus electric field (10% modulation at 100 Hz of the resonator input signal). Hysteresis cycle for the electron current is detected: triggering multipacting when there are electrons inside the resonator is easier than triggering it when there are no electrons.

2.4.3. Set-up detuning

By modulating the input power and recording the amplitude of the reflected and transmitted signals, it is possible to detect the onset of multipacting. Figure 18 shows the outline of the measurement set-up: the RF generator is operated in amplitude modulation mode, with a typical modulation index of 10%. A bi-directional coupler permits the measurement of the input power and of the reflected signal. The field amplitude inside the resonator is measured by the output coupler. The biased pickup and the electrometer allow to measure the electron current at the resonator wall. Those signals are recorded by an oscilloscope.

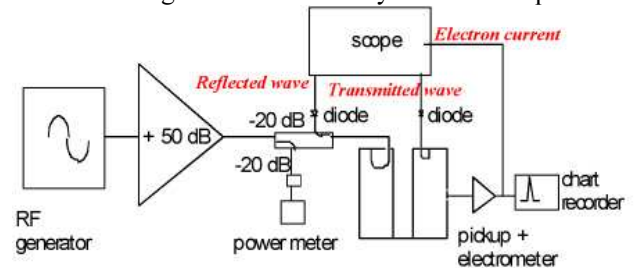


Figure 18. Layout for the measurement of the reflected and transmitted wave. After being amplified by the 50 dB power amplifier, a -20 dB directional coupler is placed between the resonator and the power amplifier. This directional coupler permits to measure the incident wave and the reflected wave produced in the resonator. The transmitted wave is measured with the output coupler, the electron current is collected by the biased pick-up and amplified by the electrometer.

Typical results are shown in Fig. 19: the time evolution of the transmitted and reflected signal, as well as the electron current are recorded while modulating amplitude without using the diodes of Fig. 18. During multipacting, the space charge due to electrons detunes the resonator and the resonant conditions are no longer fulfilled. Thus, when multipacting is triggered, transmission levels off (top trace) and reflection increases (middle trace), which is evidenced by the electron current in the pick-up (bottom trace).

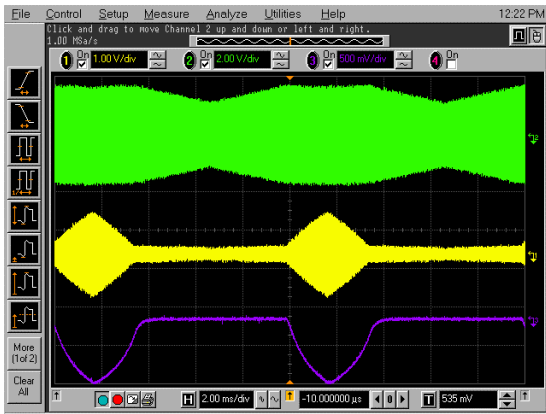


Figure 19. Time evolution of the transmitted signal (top), reflected signal (centre), and electron current (bottom), while modulating amplitude (10%). When the electric field exceeds the multipacting level, transmission becomes flat, reflection increases and electron current is collected.

2.5. Scrubbing effect for different materials

The present layout allows the comparison of multipacting level for different samples introduced in the resonator (operated in the fundamental mode). The maximum electric field is in the centre of the resonator, where the electron pick-up and the sample are located. If the multipacting level of the sample is lower than the one of stainless steel, multipacting is first produced on the sample, and then on the other parts of the resonator. In the following, we discuss measurement of multipacting level in stainless steel sample as well as ferrite and amorphous carbon (a-C).

Two different pick-up configurations are used: one to study the behaviour of the whole chamber, and one for samples of different material (Fig. 20). In the first case, the pick-up is located behind a grid of the same material as the vacuum chamber. The grid is actually a part of the outer conductor surface. Multipacting takes place on the grid, and the electrons leaving its surface pass through its holes and are collected in the electrode behind the grid. In the second pick-up configuration, the sample is supported by the pick-up itself and becomes part of the vacuum chamber wall. Hence, electrons outgoing the sample surface come back to the collector producing an electron current. In both cases, during continuous exposure, the electron dose is estimated by time integration of the pick-up current.

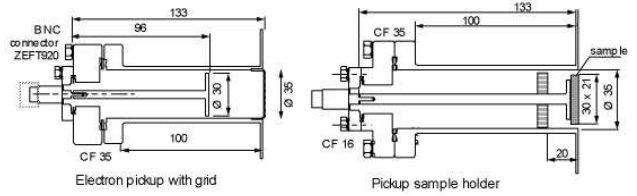


Figure 20. Pickups used to measure multipacting level of the whole chamber (left) and of samples of different materials (right). The grid used on the left pick-up is part of the outer conductor surface wall. Electrons emitted from the surface pass through the holes of the grid and reach the pick-up surface collector. On the other hand, the pick-up sample (right) forms part of the wall chamber surface and it acts also as the electron collector. Electrons emitted by the sample reach again the collector surface.

2.5.1. Scrubbing effect for stainless steel

The first step is to measure the multipacting level for the stainless steel, that is, the minimum electric field amplitude (E_0^{SS}) that will trigger the electron cloud inside the chamber. Therefore a stainless steel grid has been placed in front of the pick-up (Fig. 20) and whenever the field magnitude of E_0^{SS} is reached, the electron avalanche starts in the grid and in the surrounding area.

The minimum electric field E_0^{SS} to trigger multipacting varies after dose exposures. In Fig. 21, the electron current is plotted versus the electric field inside the resonator after 3 different electron exposures, and the multipacting level is set as the electric field corresponding to a measurable electron current. Multipacting level of "as received" stainless steel is 5.8 kV/m, but it increases with the electron dose (scrubbing effect).

This effect is well known (but not yet completely understood) as "RF conditioning" in RF devices [10]. Generally, the SEY decreases with the exposed dose [16], and thus, larger electric field amplitudes are required to trigger multipacting.

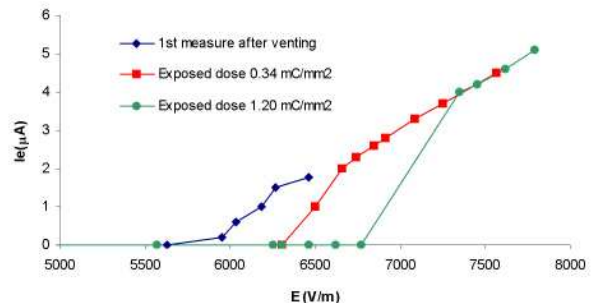


Figure 21. Electron current versus electric field amplitude for stainless steel. After different dose exposures, bigger electric field is required to trigger multipacting (scrubbing effect).

2.5.2. Scrubbing effect for ferrite sample

In the framework of the studies of the longitudinal beam coupling impedance in the LHC injection kicker model [17], it is important to evaluate the multipacting level for the ferrite used in the kicker yoke. Figure 22 shows again the current in the pick-up as a function of the resonator field: the multipacting level for ferrite is close to 1.8 kV/m, and there is no noticeable scrubbing effect (at least for this kind of ferrite) in the measured dose range (0-0.18 mC/mm²). Actually, two multipacting levels are detected: the first one (1.8 kV/m) is due to the ferrite, while the second one (5.5 kV/m) corresponds to stainless steel. Therefore it is evident that multipacting is produced first on the vertical centre of the resonator (where the ferrite is placed) and then in the other parts. It is worth noting that the multipacting level for stainless steel is slightly lower than the previous value found for stainless steel alone (5.8 kV/m) because it is easier to trigger the multipacting if there are already electrons in the resonator (similarly to the hysteresis effect mentioned in sec. 2.3).

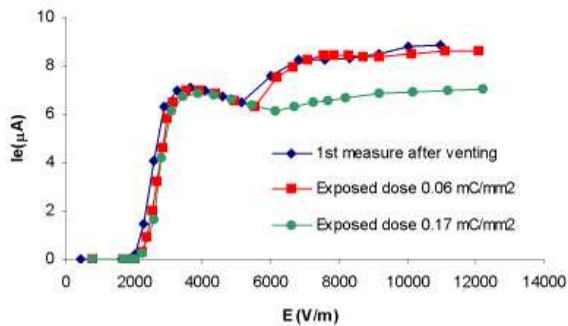


Figure 22. Electron current versus electric field amplitude for a ferrite sample. Two multipacting levels can be seen in this plot: the first one (at ~ 2 kV/m) corresponding to the ferrite sample, the second one (~ 5.5 kV/m) corresponding to the stainless steel chamber.

2.4.3. Scrubbing effect for a-C sample[†]

Other tests have been carried out on samples of Diamond type amorphous carbon (a-C), known as DLC (Diamond Like-Carbon). Such a material may be an interesting coating against multipacting since it has very good mechanical properties and it is very easy to prepare [18]. Actually a sample of a-C H-terminated diamond has been tested.

Figure 23 is analogous to Fig. 21 and 22. It shows a value of $E_0^{a-C} \cong 4.5$ kV/m independently of the exposed electron dose, which is lower than the value for stainless steel even just after venting ($E_0^{ss} = 5.8$ kV/m).

[†] Sample provided by Joan Esteve, from the Applied Physics Department of the Universitat de Barcelona.

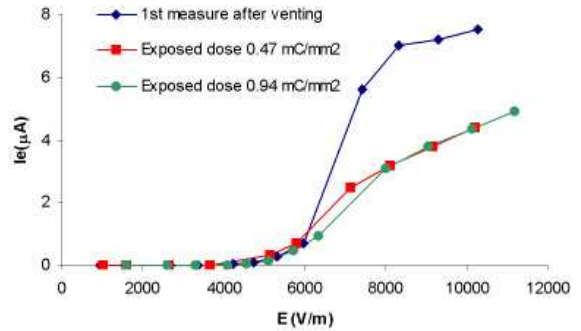


Figure 23. Electron current versus electric field amplitude for an a-C sample. No scrubbing effect is detected for this sample. However, for electric fields above its multipacting level, the electron current collected is much lower after the first electron dose, since electrons remove the first contaminated layer of the sample.

This behaviour is explained in [19] by the low electron affinity at the surface, which is mainly responsible for the high SEY from H-terminated diamond samples. Despite the fact that E_0^{a-C} does not decrease with the exposed dose, Fig. 23 shows anyway a reduction of the SEY which can be seen in terms of the collected current after the first dose: for a given value of the electric field (above the multipacting level), the electron current is significantly lower after the first dose due to the removing of the first contamination layer. The latter effect can be even probably even greater because of the rapid decrease in the yield from H-terminated diamond due to electron impingement [19]. Anyway a rigorous prove is not possible with this set-up, since part of the electron current is due to multipacting in the stainless steel. However, this material is not a good candidate to decrease multipacting due to its low multipacting level “as received”, and due to the weak scrubbing effect detected.

2.5.4. Scrubbing effect for a Non Evaporable Getter (NEG) coating

In a getter coated beam pipe one expects the electron cloud build-up to be strongly decreased. In the framework of the studies of the electron cloud in the SPS, a NEG (TiZrV) coated vacuum chamber has been tested in this set-up, as planned in [20]. Coating the whole inner surface of the outer conductor (including the grid) avoids the effect of two multipacting levels taking place at the same time inside the resonator (as occurred for ferrite and a-C samples).

When NEG is not activated (i.e. heated at 200°C for 24 hours), there is a clear electron cloud build up and a consistent scrubbing effect. Figure 24 shows this effect in the same way as Fig. 21. However, when activated, there is no electron signature inside the resonator (no electron current, no changes in transmitted and/or

reflected waves), but the pressure increase is nevertheless not negligible. Thus such a pressure increase can not be explained by electron multipacting, but it may be due to some thermal effect or other RF breakdown mechanism.

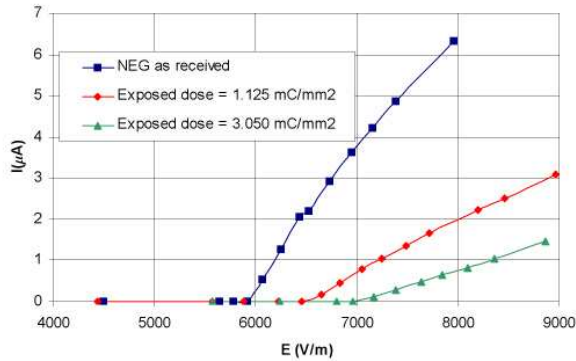


Figure 24. Electron current versus amplitude of the electric field for a non activated NEG coating in a vacuum chamber. With the exposed dose, the electron current decreases and multipacting level increases, evidencing the scrubbing effect for a non activated NEG.

Figure 25 clearly shows that transmission and pressure rise are not correlated. It should be mentioned that NEG usually reaches pressures around 10^{-11} mbar after activation; such low pressures were not obtained when the measurement took place (see Fig. 25), possibly indicating a non proper activation process.

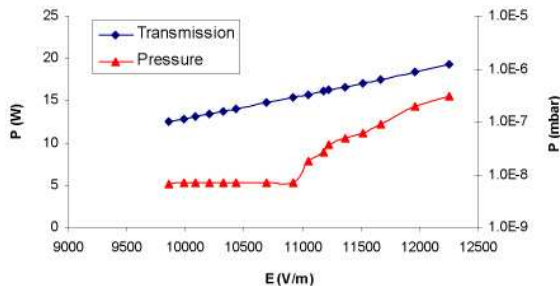


Figure 25. Transmitted power and pressure inside the resonator versus electric field amplitude for an activated NEG coating inside the resonator. After activation, the NEG coating does not show any multipacting signatures. Only a pressure increase, likely not due to multipacting since no electron current and no limitation in transmission signal are detected.

2.6. Conclusions

The coaxial resonator set-up allows the production of high electric fields and the generation of the high electron doses needed to properly study the behaviour of materials submitted to multipacting and thus it is a suitable test bench for electron cloud studies. We have demonstrated qualitatively how the resonator changes its resonant conditions when multipacting takes place.

The resonator detunes while electron current is detected on the pick-up: transmitted signal levels off and reflected signal increases suddenly. The appearance of the hysteresis cycle in the collected electron current after proper modulation of the input power, shows that the effect continues at electric fields lower than needed to start it.

It is possible to measure the onset of multipacting and its variations with the exposed dose of electrons, which makes it an effective tool to study the scrubbing effect for different samples. No scrubbing effect was evidenced in ferrite (at least in the applied dose range), while for a-C the scrubbing effect cannot be identified by the multipacting level but only in the collected electron current at higher electric fields. For stainless steel, scrubbing effect has been shown clearly. Also a NEG (TiZrV) coated vacuum chamber has been tested in this set-up. After activation, preliminary results do not show any evidence of electron multipacting (no electron current, no changes in transmitted and/or reflected signal are detected) but only a pressure rise. The reason can be found in a thermal effect or other form of RF breakdown due to the high power introduced in the set-up, but further studies are needed to explain this effect.

In the framework of the electron cloud program carried out at CERN, a computer code is going to be developed to simulate multipacting in this set-up. Checking simulation results with measurements in the laboratory will be a useful tool to understand this phenomenon. Further surface treatments (TiN and ArGD) are going to be tested as coatings against multipacting in this set-up, which is becoming a useful test bench for electron cloud studies.

3. REFERENCES

- [1]. M. Pivi. Beam induced electron multipacting in the LHC. PhD Thesis. CERN – University of Torino. Geneva, May 2000.
- [2]. F. Ruggiero et al. Beam-induced electron cloud in the LHC and possible remedies. Geneva-CERN. In: 6th European Particle Accelerator Conference, Stockholm, Sweden, Jun 1998 - IOP, 1999. - pp.359-361
- [3]. H.H. Braun et al., The CLIC RF power source: a novel scheme of two beam acceleration for e^\pm Linear colliders, CERN Clic Note 864 (unpublished).
- [4]. Matthaei, GL; Young; L and Jones, EMT. Microwave filters, impedance-matching networks and coupling structures. Ed. by Artech house books, section 14.05.
- [5]. Zinke and Brunswig. Hochfrequenztechnik I. Ed. Auflage.
- [6]. Harlan Howe, JR. Stripline circuit design. Ed. by Artech house, Inc. Ch 5.
- [7]. A. Lombardi, private communications.
- [8]. Zinke, O. and Brunswig, H. Lehrbuch der Hochfrequenztechnik. Chap. 3. New York 1973.

- [9]. Cristal, E.G. and Young, L. IEEE Transaction on microwave theory and techniques. Pg 544-558, September 1965.
- [10]. H. Padammsee, T. Hays and J. Knobloch. RF Superconductivity for accelerators. Ed. Wiley Interscience publications.
- [11]. O. Brüning, F. Caspers, J.-M. Laurent, M. Morvillo, and F. Ruggiero. Multipacting tests with magnetic field for the LHC beam screen. LHC project report 187, June 1998.
- [12]. CAS - RF engineering for particle accelerators. April 1991, Oxford, UK. Proceedings edited in Geneva 1992, CERN.
- [13]. F. Caspers private communications.
- [14]. U. Iriso et al. Improvements on the Traveling Wave chamber for multipacting simulations. Vac. Tech. Note, 01-17. November 2001.
- [15]. G.Arduini et al. Electron cloud: observations with LHC-type beams in the SPS. Presented in EPAC 2000, Vienna, Austria. June 2000.
- [16]. N.Hilleret et al. Electron cloud and beam scrubbing in the LHC. Presented at PAC 1999, New York City, NY, USA. April 1999. Ed. by Luccio, A and MacKay, W W - IEEE Computer Society Press, Piscataway, NJ, 1999.
- [17]. F. Caspers, C. Gonzalez, H. Tsutsui and M. D'yachkov. Impedance measurements on the LHC

injection kicker prototype. LHC project note, March 2000.

[18]. J. Esteve, F.J. Pino, J.L. Andújar. Obtención de recubrimientos de carbono amorfo tipo diamante. Presented in TRATERMAT 2000, Barcelona, Spain. June 2000.

[19]. A. Shih, J. Yater, C. Hor, R. Abrams. Secondary electron emission studies. Applied Surface Science 111 (1997), 251-258.

[20]. Conceptual design review of the room temperature parts of the beam vacuum system for the long straight sections for the LHC. Engineering report. LHC project document, March 2002.

4. ACKNOWLEDGMENTS

P. Griessen supplied the feedthroughs from the SWC-LEP; H.Kos and D. Collet machined precisely the pieces we were looking for; A. Lombardi gave the idea and help with using *Superfish*; C. Deibele (Oak Ridge National Laboratories, US) substantially helped with the calculations of the coupling factor with *SERENADE*; J. Esteve and the Applied Physics Department from the Universitat de Barcelona provided the a-C samples. Eventually, many thanks to all the LHC/VAC group for their support; and F. Ruggiero, G. Rumolo and F. Zimmermann for their encouragements.